



Energy dissipation of wind-generated waves and whitecap coverage

Paul A. Hwang¹ and Mark A. Sletten¹

Received 9 April 2007; revised 27 September 2007; accepted 20 November 2007; published 14 February 2008.

[1] The energy dissipation per unit area of the ocean surface attributed to fetch- or duration-limited wind-generated waves can be expressed in terms of wind speed, significant wave height and peak wave frequency. Such a parameterization equation can be exploited for obtaining a first order estimation of the rate of energy input through the air-sea interface in the world's oceans using satellite output of wind speed, wave height and wave period. For general wind wave events in the ocean with event duration longer than one hour, the energy dissipation (in W/m^2) is equal to the product of the density of air, wind speed cubed and a proportionality coefficient between 0.00037 and 0.00057. Using the equation to calculate the wave energy dissipation, the whitecap coverage is proportional linearly to the energy dissipation. The threshold energy dissipation for whitecap inception is between 0.013 and 0.038 W/m^2 , which corresponds to a threshold wind speed of between 2.5 and 3.6 m/s. The proportionality coefficient is relatively constant for a wide range of wave growth conditions in comparison to the data scatter in the whitecap measurements. This may explain why it is so difficult to establish an unequivocal dependence on the explicit surface wave parameters in the whitecap data. The weak explicit wave signal can be detected after the cubic wind speed dependence is removed.

Citation: Hwang, P. A., and M. A. Sletten (2008), Energy dissipation of wind-generated waves and whitecap coverage, *J. Geophys. Res.*, 113, C02012, doi:10.1029/2007JC004277.

1. Introduction

[2] Wind-generated waves are the ocean surface roughness. Mass, momentum and energy passing through the air-sea interface under a given wind condition are modified by surface wave conditions. A useful parameter of wind waves in the study of air-sea exchange is the dissipation function because it quantifies the work done by the wind to the ocean. In many situations detailed wave spectral information is not available, and parameterization of energy dissipation with some global representation of surface waves, such as the significant wave height and dominant wave period, is of great value. In particular, satellite remote sensing using scatterometers, radiometers, altimeters and synthetic aperture radars is now approaching the stage of providing global coverage of wind speed, significant wave height and dominant wave period. A parameterized energy dissipation equation can be used to generate a synoptic estimation of the energy input at the air-sea interface, which is an important upper boundary condition of ocean fluid dynamics and lower boundary condition of atmospheric circulation.

[3] Source function investigation is one of the most challenging tasks in wind wave research. The dominant source terms of ocean surface waves are wind input,

breaking dissipation, and nonlinear wave-wave interaction. Nonlinear interaction causes energy exchanges between wave spectral components and does not contribute to the overall energy gain or loss of the wavefield. To obtain the overall energy budget of the wavefield, one can integrate the spectral energy equation over the frequency or wave number space to remove the nonlinear interaction term. Several field measurement programs have yielded useful parameterization functions of the wind generation function [e.g., Snyder *et al.*, 1981; Hsiao and Shemdin, 1983; Donelan *et al.*, 2006] and an empirical expression of the integrated wind input can be readily derived. The fetch- or duration-limited growth laws can be used to derive a resultant source term, that is, the net growth rate of wind waves. The difference between the integrated wind input and the net wave growth, therefore, represents the integrated energy dissipation. As shown in the next section, the net growth rate is one order of magnitude smaller compared to the wind input [see also Hasselmann *et al.*, 1973; Donelan, 1998], for practical purposes, the integrated energy dissipation can be approximated with the integrated wind input. The detailed discussion is presented in section 2. The practice of equating wind input to breaking dissipation is also adapted by Phillips [1985] to derive an analytical solution for the total energy dissipation of a wind-generated wavefield in equilibrium state. He obtains the total dissipation rate by integrating the spectral dissipation function over the wave number range of the equilibrium spectrum. The upper and lower bounds of the equilibrium range are

¹Remote Sensing Division, Naval Research Laboratory, Washington, DC, USA.

suggested to be from the spectral peak wave number to an upper cutoff wave number determined by the surface drift, which is eventually estimated to be some large multiple of the spectral peak wave number. (See also the discussion by *Hwang and Wang* [2001, section 3] on the wave number range of the equilibrium spectrum based on field measurements of mean square slopes and wave components participated in nonlinear interaction.) His solution technique has been used to compute the breaking wave energy dissipation using the in situ measured wave spectrum in addition to the assumed equilibrium spectrum [*Felizardo and Melville*, 1995; *Hanson and Philips*, 1999]. *Gemmrich and Farmer* [2004] report near surface turbulence measurements in the presence of breaking waves using acoustic sensors mounted on a floating structure. *Agrawal et al.* [1992] and *Terray et al.* [1996] present results of the vertical distribution of the energy dissipation calculated from the velocity spectra measured by laser Doppler anemometer, acoustic sensor and drag sphere. An important conclusion from these field measurements is that the energy dissipation in the upper ocean layer is one to two orders of magnitude greater than that predicted by the wall layer similarity. A very good agreement is found in the comparison of the total energy dissipation calculated with the simple parameterization function using the global wind and wave parameters obtained in this paper and the results calculated using Phillips's spectral solution as well as the total dissipation integrated from the vertical profile of the energy dissipation functions established in the latter experiments (section 2.4).

[4] In section 3, the derived dissipation function is applied to the whitecap observations that also reported wave measurements. Over the years, extensive observations of whitecaps have led to the conclusion that the power law wind speed dependence remains the most robust empirical relation describing the whitecap coverage in the ocean despite the consensus that wave parameters somehow play a role because whitecaps are caused by wave breaking, thus it should be related to wave energy dissipation [e.g., *Monahan*, 1971; *Toba and Chaen*, 1973; *Ross and Cardone*, 1974; *Monahan and O'Muircheartaigh*, 1986; *Wu*, 1988; *Zhao and Toba*, 2001; *Lafon et al.*, 2004, 2007; *Anguelova and Webster*, 2006]. With the analytical expression of the integrated energy dissipation, it becomes clear that wave energy dissipation is proportional to the cubic power of wind speed and the explicit dependence on wave parameters is $\omega_*^{3.3} \eta_*$, which varies only slightly for a wide range of wave development conditions ($\omega_* = \omega_p U/g$ and $\eta_* = \eta_{rms}^2 g^2/U^4$ are dimensionless reference wave frequency and wave variance, respectively, ω_p the spectral peak frequency, U the neural wind speed at 10 m elevation, η_{rms}^2 the variance of surface displacement and g the gravitational acceleration). The weak explicit dependence on the wave parameters is buried in the large data scatter in the whitecap measurements and the strong cubic wind speed relationship. This offers a plausible explanation on why it is so difficult to establish a reliable dependence of the whitecap coverage on wave parameters up to this date. The weak signal of explicit wave dependence can be detected when the whitecap

coverage is divided by the wind speed cubed. A summary is presented in section 4.

2. Derivation of the Dissipation Function

2.1. Basic Approach

[5] The balance of wind-generated surface wave energy spectral density, $\chi(\omega)$, in deep water can be written as

$$\frac{d\chi(\omega)}{dt} = Q_{in} + Q_{nl} + Q_{dis}, \quad (1)$$

where Q_{in} , Q_{nl} and Q_{dis} are the wind input, nonlinear interaction and dissipation source functions. As stated in the Introduction section, here we seek parameterization of the total energy balance integrated over the frequency or wave number range. As a result, the nonlinear wave-wave interaction term vanishes and (1) is reduced to

$$\frac{dS}{dt} = \langle Q_{in} \rangle + \langle Q_{dis} \rangle, \quad (2)$$

where S is the variance of surface elevation, η_{rms}^2 , and angle brackets represent spectral average. Our progress in the theoretical and experimental study of the wind input function is considerably more advanced than that of the breaking dissipation function and several different parameterizations of Q_{in} , with support of experimental data of simultaneous measurements of near-surface pressure and elevation, have been suggested (section 2.2). In comparison, measurement of wave dissipation is a very difficult task and the parameterization of dissipation function is primarily deduced from balancing the wind input and nonlinear interaction terms in numerical wave models.

[6] A different source of data for investigating the wave energy balance is duration- or fetch-limited wave growth functions. In such measurements, the individual source functions cannot be separated and the equation can be written as

$$\frac{dS}{dt} = \langle Q_{net} \rangle, \quad (3)$$

where Q_{net} is the net source function. Because nonlinear wave-wave interaction causes energy exchanges among different wave components, the spectral average $\langle Q_{nl} \rangle = 0$, and $\langle Q_{net} \rangle$ can be equated to the residual of $\langle Q_{in} \rangle$ and $\langle Q_{dis} \rangle$. Theoretical discussions and empirical measurements suggest that the wave development subject to wind input or net source function is exponential (with non-constant growth rate, see section 2.3), thus we can express these source terms as

$$\langle Q_x \rangle = \langle \gamma_x \rangle s \omega_p S, \quad (4)$$

where the dimensionless coefficient $\langle \gamma_x \rangle$ can be $\langle \gamma_{in} \rangle$ or $\langle \gamma_{net} \rangle$ for $\langle Q_{in} \rangle$ or $\langle Q_{net} \rangle$, respectively, and $s = \rho_a / \rho_w$ the ratio of air and water densities. The wave variance is related to the total wave energy per unit area of the ocean surface by $E = \rho_w g H_s^2 / 8 = 2 \rho_w g \eta_{rms}^2$, $H_s = 4 \eta_{rms}$ is the significant wave height and g the gravitational acceleration [e.g., *Dean and Dalrymple*, 1991]. In the following calculations, s equal

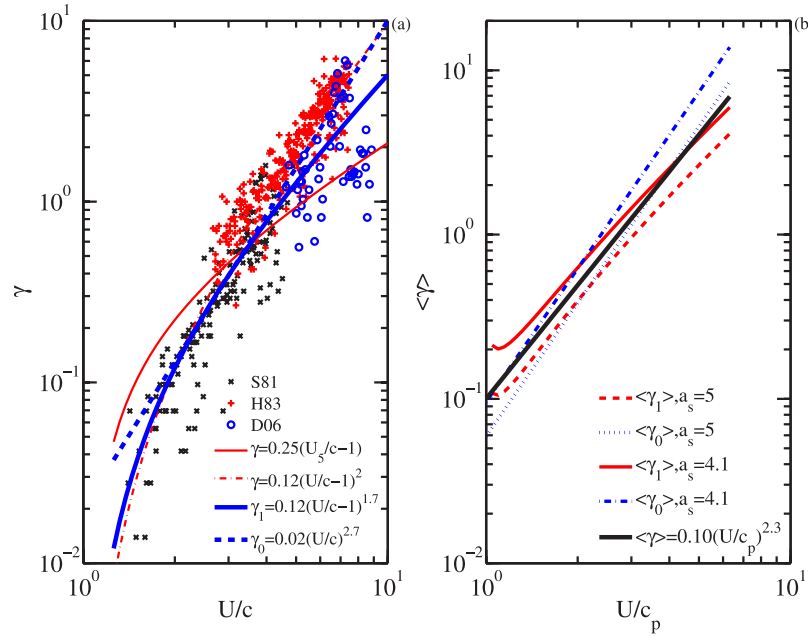


Figure 1. (a) Wind input data obtained from field environments [Snyder *et al.*, 1981; Hsiao and Shemdin, 1983; Donelan *et al.*, 2006]. Also shown are the fitting functions proposed by the individual authors and from least squares fitting of the combined data. (b) The integrated wind input coefficient computed with different spectral slopes and fitting functions of wind input coefficient.

to 1/858, which is obtained with $\rho_w = 1030 \text{ kg/m}^3$ for seawater and $\rho_a = 1.20 \text{ kg/m}^3$ for air at 20°C [Beranek, 1988].

[7] As will be illustrated in section 2.3, empirical data show that $\langle \gamma_{net} \rangle$ is one order of magnitude smaller than $\langle \gamma_{in} \rangle$ (about 5 to 10%), and given the large uncertainty of the latter quantity (on the order of 100%), it is justifiable to equate $\langle \gamma_{dis} \rangle$ with $\langle \gamma_{in} \rangle$. From this point on, both input and dissipation coefficients will be represented simply by $\langle \gamma \rangle$. Using (4) and the normalization factors g and U , the energy dissipation of wind waves, $\varepsilon = \langle 2\rho_w g Q_{dis} \rangle$, can be written in dimensionless form of wind and wave parameters as

$$\frac{\varepsilon}{\rho_a U^3} = 2\langle \gamma \rangle \omega_* \eta_* . \quad (5)$$

The neutral wind speed at 10 m elevation, U_{10} , is employed as the reference wind speed. The subscript of wind speed will be dropped for simplicity unless clarification is necessary. Thus $\eta_* = \eta_{rms}^2 g^2 / U^4$ and $\omega_* = \omega_p U / g$ as stated earlier.

2.2. Wind Input

[8] Figure 1a displays field measurements of the wind input coefficient reported by Snyder *et al.* [1981], Hsiao and Shemdin [1983] and Donelan *et al.* [2006]. These data are digitized from their Figure 6, Figure 4, and Figure 7, respectively. Snyder *et al.* [1981] and Donelan *et al.* [2006] present their results with a reference wind speed at 5 m elevation, U_5 , which is converted to U_{10} using a multiplication factor of 1.06, corresponding to a drag coefficient $C_d = 1.2 \times 10^{-3}$, or equivalently, a dynamic roughness $z_0 = 10^{-4} \text{ m}$, and a logarithmic wind speed profile.

[9] Snyder *et al.* [1981] suggest that their data can be represented by the following linear function of the ratio between wind speed and wave phase speed, c ,

$$\gamma = \frac{1}{s\omega\chi} \frac{d\chi}{dt} \sim (0.2 \text{ to } 0.3) \left(\frac{U_5}{c} - 1 \right), \quad (6)$$

where χ is the wave frequency spectral density and γ the growth rate of the spectral component. In Figure 1a the curve $\gamma = 0.25(U_5/c - 1)$ is plotted. The function underpredicts the growth rate at higher U/c region when compared to the measurements of Hsiao and Shemdin [1983] but it goes through the middle of the data cluster of Donelan *et al.* [2006].

[10] Hsiao and Shemdin [1983] offer the following function based on the combined data of their own and those of Snyder *et al.* [1981],

$$\gamma = 0.12 \left(\frac{U}{c} - 1 \right)^2 . \quad (7)$$

The curve lies near the upper bound of the data clusters of Snyder *et al.* [1981] and Donelan *et al.* [2006]. These three sets of field data are combined and least squares power law fitting yields the following equation based on $U/c - 1$,

$$\gamma_1 = 0.12 \left(\frac{U}{c} - 1 \right)^{1.7} . \quad (8)$$

Least squares power law fitting based on U/c produces

$$\gamma_0 = 0.02 \left(\frac{U}{c} \right)^{2.7} . \quad (9)$$

All fitting curves (6) to (9) are shown with the data in Figure 1a.

[11] To facilitate computation using global wave parameters, an integrated wind input function is defined by

$$\langle \gamma \rangle = \frac{\int_{\omega_p}^{N\omega_p} \gamma s \omega \chi(\omega) d\omega}{s \omega_p \eta_{rms}^2}. \quad (10)$$

[12] Spectral analysis of air-sea energy and momentum input shows that the dominant contribution of wind input is from wave components above the spectral peak frequency [e.g., *Makin et al.*, 1995; *Donelan*, 1998], the integration is carried out from the spectral peak frequency, ω_p , to an upper limit defined by $N\omega_p$ with $N > 1$. The spectral function in this frequency range is assumed to be a power law function $\chi(\omega) = A_s \omega^{-a_s}$. The detail is described in Appendix A. The quantitative value of the integrated wind input function depends on the assumption of the spectral slope and the frequency bandwidth of integration. Figure 1b shows the computed $\langle \gamma \rangle$ as a function of ω_* for two different spectral slopes, -4.1 and -5 . $N = 5$ is used here for the upper cutoff frequency. In a study of the ocean surface roughness, *Hwang and Wang* [2001] present a discussion suggesting that the frequency bandwidth of the equilibrium range of surface wave spectrum is about $2.5\omega_p$ based on observations of ocean surface mean square slopes and the consideration of wave number components involved in nonlinear wave-wave interaction. The integration here is carried out over a frequency range about twice the equilibrium bandwidth. A sensitivity analysis on the integration frequency bandwidth is presented in Appendix A. The difference between using γ_1 and γ_0 for the same spectral slope appears in the rate of change of $\langle \gamma \rangle$ with respect to U/c_p ; with γ_1 , $\langle \gamma_1 \rangle \sim (U/c_p)^2$, and with γ_0 , $\langle \gamma_0 \rangle \sim (U/c_p)^{2.7}$. (Note, U/c_p and ω_* are identical for deep water waves.) Overall, the average can be approximated by

$$\langle \gamma \rangle = 0.10 \left(\frac{U}{c_p} \right)^{2.3} = 0.10 \omega_*^{2.3}. \quad (11)$$

With the combinations of short wave spectral slope of 4.1 or 5 and empirical fitting of wind input function expressed in either γ_1 or γ_0 , the data scatter in the integrated wind input is estimated to be about a factor of two (Figure 1b). In comparison, the typical data scatter of energy dissipation rate measurements and related properties such as whitecap observations is about one to two orders of magnitude worse.

2.3. Net Growth Rate

[13] The net growth rate of wind generated waves can be estimated from empirical wave growth observations. Using the JONSWAP fetch-limited growth functions, *Hasselmann et al.* [1973] estimate that the net momentum retained in the wavefield is about five percent of the wind input. The air-sea momentum flux is calculated with a constant drag coefficient of 0.001. They also perform computation of nonlinear wave-wave interaction using the JONSWAP spectrum. For short fetch conditions, about five percent of momentum flux across the air-sea interface remains in the wavefield while more than 90 percent is transferred by

wave-wave interaction to shorter waves and then passed to currents through dissipation. For medium to long fetches, they comment that there are ambiguities in the nonlinear interaction computation of the fraction of momentum retained in the wavefield.

[14] *Donelan* [1998] computes the wind input of energy and momentum integrated over the directional spectral function given by *Donelan et al.* [1985] using a growth rate function described by *Donelan and Pierson* [1987]. The net growth rate is calculated with the fetch growth laws derived from a field study conducted in Lake Ontario [*Donelan et al.*, 1992]. The fraction of energy and momentum retained in the wavefield is found to be less than four percent of the total wind input, and there is a generally decreasing trend toward more mature wave age.

[15] *Hwang and Wang* [2004] and *Hwang* [2006] developed a technique to process fetch limited wave growth data with polynomial functions of the logarithmic of the dimensionless fetch. To the first order the result yields the simple power law functions. Extending to the second order, the polynomial functions improve the agreement with the data trend considerably, especially for both younger and more mature seas. The fetch-limited growth functions can be written as

$$\eta_* = Ax_*^a; \quad \omega_* = Bx_*^b; \quad \eta_* = R\omega_*^r, \quad (12)$$

where x is distance (fetch) and $x_* = xg/U^2$. The growth functions have also been converted to the temporal domain to represent duration-limited growth,

$$\eta_* = Pt_*^p; \quad \omega_* = Qt_*^q, \quad (13)$$

where t is time (duration) and $t_* = tg/U$. For the first order fitting, A , a , B , b , P , p , Q , q , R and r are constant. For the second order fitting, they vary with the stage of wave growth, that is, dimensionless duration, fetch or reference frequency [*Hwang and Wang*, 2004; *Hwang*, 2006]. The computation of the coefficients and exponents for the second order growth functions is somewhat tedious. For convenience, lookup tables with x_* in logarithmic scale are provided in Table 1.

[16] The net growth rate can be derived from substituting (4) into (2) with the aid of the second order fitted growth functions (13),

$$\langle \gamma_{net} \rangle = \frac{\rho_w P^{\frac{1}{p}} p \eta_*^{\frac{1}{p}} \omega_*^{-1}}{\rho_a}. \quad (14)$$

[17] Figure 2 shows the ratio between the net growth rate and the integrated wind input shown in Figure 1b. The magnitude of $\langle \gamma_{net} \rangle$ is about one order of magnitude smaller than $\langle \gamma \rangle$ and it varies somewhat with the assumption of the short wave spectral slope, a_s . For young waves with $a_s = 5$, the ratio is generally less than 13%, and with $a_s = 4.1$, it is generally less than 8%. This ratio drops rapidly in the region of $U/c_p < 2$ where most of field data exist.

2.4. Energy Dissipation

[18] The results from the studies of fetch- and duration-limited growth functions [e.g., *Hasselmann et al.*, 1973;

Table 1. Lookup Tables for the Fetch- and Duration-Limited Growth Functions

(a) Fetch-limited									(b) Duration-limited								
x_*	ω_*	A	a	B	b	100R	r	η_*	t_*	ω_*	P	p	Q	q	100R	r	η_*
1.00e0	20.857	2.236e-8	1.765	20.857	-0.399	1.527	-4.422	2.236e-8	8.68e1	20.857	4.558e-14	2.936	403.734	-0.664	1.527	-4.422	2.236e-8
1.58e0	17.397	2.267e-8	1.705	20.809	-0.389	1.365	-4.384	4.972e-8	1.13e2	17.397	9.357e-14	2.790	351.845	-0.636	1.365	-4.384	4.972e-8
2.51e0	14.578	2.363e-8	1.645	20.663	-0.379	1.222	-4.344	1.075e-7	1.47e2	14.578	1.945e-13	2.648	305.917	-0.610	1.222	-4.344	1.075e-7
3.98e0	12.274	2.530e-8	1.586	20.424	-0.369	1.095	-4.302	2.263e-7	1.93e2	12.274	4.091e-13	2.511	265.395	-0.584	1.095	-4.302	2.263e-7
6.31e0	10.382	2.785e-8	1.526	20.093	-0.358	0.983	-4.257	4.632e-7	2.55e2	10.382	8.705e-13	2.379	229.751	-0.559	0.983	-4.257	4.632e-7
1.00e1	8.822	3.152e-8	1.467	19.676	-0.348	0.883	-4.210	9.227e-7	3.38e2	8.822	1.873e-12	2.250	198.487	-0.535	0.883	-4.210	9.227e-7
1.58e1	7.532	3.665e-8	1.407	19.177	-0.338	0.795	-4.160	1.788e-6	4.51e2	7.532	4.071e-12	2.126	171.140	-0.511	0.795	-4.160	1.788e-6
2.51e1	6.461	4.381e-8	1.347	18.604	-0.328	0.717	-4.107	3.372e-6	6.04e2	6.461	8.942e-12	2.005	147.282	-0.488	0.717	-4.107	3.372e-6
3.98e1	5.568	5.382e-8	1.288	17.965	-0.318	0.648	-4.050	6.185e-6	8.12e2	5.568	1.983e-11	1.888	126.519	-0.466	0.648	-4.050	6.185e-6
6.31e1	4.821	6.796e-8	1.228	17.266	-0.308	0.587	-3.990	1.104e-5	1.10e3	4.821	4.440e-11	1.774	108.493	-0.445	0.587	-3.990	1.104e-5
1.00e2	4.193	8.820e-8	1.169	16.517	-0.298	0.533	-3.926	1.917e-5	1.49e3	4.193	1.003e-10	1.664	92.877	-0.424	0.533	-3.926	1.917e-5
1.58e2	3.665	1.177e-7	1.109	15.728	-0.288	0.485	-3.857	3.239e-5	2.04e3	3.665	2.287e-10	1.557	79.380	-0.404	0.485	-3.857	3.239e-5
2.51e2	3.218	1.613e-7	1.049	14.906	-0.277	0.443	-3.783	5.324e-5	2.80e3	3.218	5.256e-10	1.452	67.737	-0.384	0.443	-3.783	5.324e-5
3.98e2	2.838	2.273e-7	0.990	14.062	-0.267	0.405	-3.703	8.515e-5	3.86e3	2.838	1.218e-09	1.351	57.714	-0.365	0.405	-3.703	8.515e-5
6.31e2	2.516	3.293e-7	0.930	13.203	-0.257	0.373	-3.617	1.325e-4	5.34e3	2.516	2.845e-09	1.252	49.102	-0.346	0.373	-3.617	1.325e-4
1.00e3	2.240	4.902e-7	0.871	12.340	-0.247	0.344	-3.524	2.006e-4	7.44e3	2.240	6.697e-09	1.156	41.716	-0.328	0.344	-3.524	2.006e-4
1.58e3	2.004	7.500e-7	0.811	11.479	-0.237	0.319	-3.424	2.954e-4	1.04e4	2.004	1.588e-08	1.063	35.393	-0.310	0.319	-3.424	2.954e-4
2.51e3	1.801	1.180e-6	0.751	10.628	-0.227	0.297	-3.314	4.233e-4	1.46e4	1.801	3.792e-08	0.972	29.988	-0.293	0.297	-3.314	4.233e-4
3.98e3	1.626	1.907e-6	0.692	9.795	-0.217	0.279	-3.194	5.902e-4	2.07e4	1.626	9.119e-08	0.883	25.376	-0.277	0.279	-3.194	5.902e-4
6.31e3	1.475	3.168e-6	0.632	8.985	-0.207	0.263	-3.062	8.006e-4	2.93e4	1.475	2.207e-07	0.797	21.447	-0.260	0.263	-3.062	8.006e-4
1.00e4	1.344	5.410e-6	0.573	8.204	-0.196	0.250	-2.916	1.057e-3	4.18e4	1.344	5.378e-07	0.713	18.104	-0.244	0.250	-2.916	1.057e-3
1.58e4	1.231	9.495e-6	0.513	7.455	-0.186	0.241	-2.755	1.357e-3	5.99e4	1.231	1.318e-06	0.631	15.265	-0.229	0.241	-2.755	1.357e-3
2.51e4	1.132	1.713e-5	0.454	6.744	-0.176	0.233	-2.575	1.695e-3	8.63e4	1.132	3.252e-06	0.550	12.856	-0.214	0.233	-2.575	1.695e-3
3.98e4	1.047	3.176e-5	0.394	6.072	-0.166	0.230	-2.373	2.060e-3	1.25e5	1.047	8.068e-06	0.472	10.816	-0.199	0.230	-2.373	2.060e-3
6.31e4	0.972	6.053e-5	0.334	5.441	-0.156	0.229	-2.145	2.436e-3	1.82e5	0.972	2.013e-05	0.396	9.090	-0.185	0.229	-2.145	2.436e-3
1.00e5	0.907	1.186e-4	0.275	4.853	-0.146	0.233	-1.885	2.803e-3	2.65e5	0.907	5.051e-05	0.322	7.631	-0.171	0.233	-1.885	2.803e-3
1.58e5	0.850	2.387e-4	0.215	4.309	-0.136	0.242	-1.587	3.138e-3	3.90e5	0.850	1.274e-04	0.249	6.401	-0.157	0.242	-1.587	3.138e-3
2.51e5	0.800	4.940e-4	0.156	3.808	-0.125	0.259	-1.240	3.417e-3	5.75e5	0.800	3.231e-04	0.178	5.363	-0.143	0.259	-1.240	3.417e-3
3.98e5	0.757	1.051e-3	0.096	3.349	-0.115	0.287	-0.832	3.621e-3	8.52e5	0.757	8.234e-04	0.108	4.489	-0.130	0.287	-0.832	3.621e-3
6.31e5	0.720	2.297e-3	0.036	2.932	-0.105	0.333	-0.346	3.733e-3	1.27e6	0.720	2.109e-03	0.041	3.755	-0.118	0.333	-0.346	3.733e-3
1.00e6	0.687	5.161e-3	-0.023	2.555	-0.095	0.410	0.244	3.744e-3	1.90e6	0.687	5.427e-03	-0.026	3.138	-0.105	0.410	0.244	3.744e-3

Donelan, 1998; Hwang and Wang, 2004; Hwang, 2006] have led to the conclusion that the net growth rate is about one order of magnitude less than the wind input. It is therefore justified to approximate the integrated wave dissipation function with the integrated wind input (11) in the present effort seeking to establish a parameterized dissipation function using wind speed and basic wave properties. The energy dissipation of wind waves (5) becomes

$$\varepsilon = \alpha \rho_a U^3, \text{ with } \alpha = 0.20 \omega_*^{3.3} \eta_*. \quad (15)$$

As noted earlier in section 2.1, the accuracy of α is estimated to be within about a factor of two. The uncertainty of the dissipation rate from the present approach is caused mainly by our imperfect knowledge of the wind input function and the short wave spectral function (Figure 1b).

[19] Figure 3a shows the variation of α as a function of wave development, which can be characterized by the dimensionless reference frequency; note that for deep water wave conditions ω_* is identically the inverse wave age, $1/(c_p/U)$. As the waves develop (from large to small ω_*) α gradually increases and reaches a maximum near $\omega_* = 1.8$ and then decreases as the waves become more mature, less choppy and eventually outrun the wind field. This curve can be interpreted as the temporal evolution of wave energy dissipation under forcing by a constant wind speed. Figure 3b illustrates the temporal evolution of ω_* under duration-limited wave growth for $U = 5, 10, 15$ and 20 m/s. Combining the results of Figures 3a and 3b, we can obtain the temporal average $\langle \alpha \rangle$ for different wind speeds of various

wind durations (Figure 3c), where $\langle \alpha \rangle = (\int_0^T \alpha dt)/T$ and T the duration of wind event. The magnitude of $\langle \alpha \rangle$ at a given duration of a wind event is wind speed dependent: for example, it varies from about 3.2×10^{-4} at the young stage to 5.7×10^{-4} at a more mature stage for $U = 5$ m/s, and from about 1.5×10^{-4} to 5.7×10^{-4} for $U = 20$ m/s. For common wind events in the ocean with wind duration longer than one hour, the numerical value of $\langle \alpha \rangle$ for practical

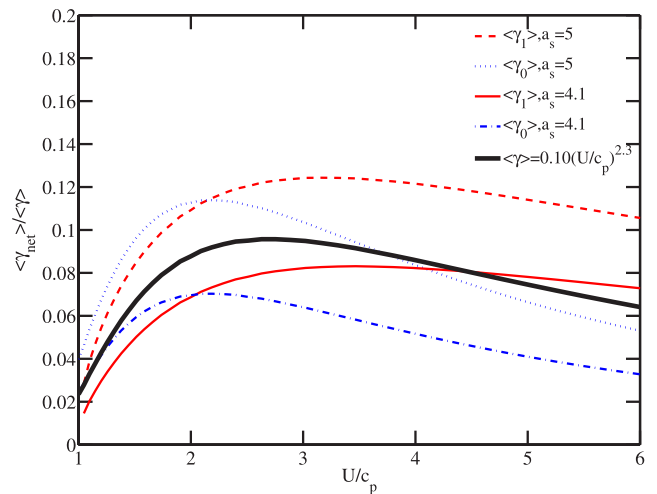


Figure 2. The ratio between the net growth rate and the integrated wind input coefficient computed with different spectral slopes and fitting functions of wind input coefficient shown in Figure 1b.

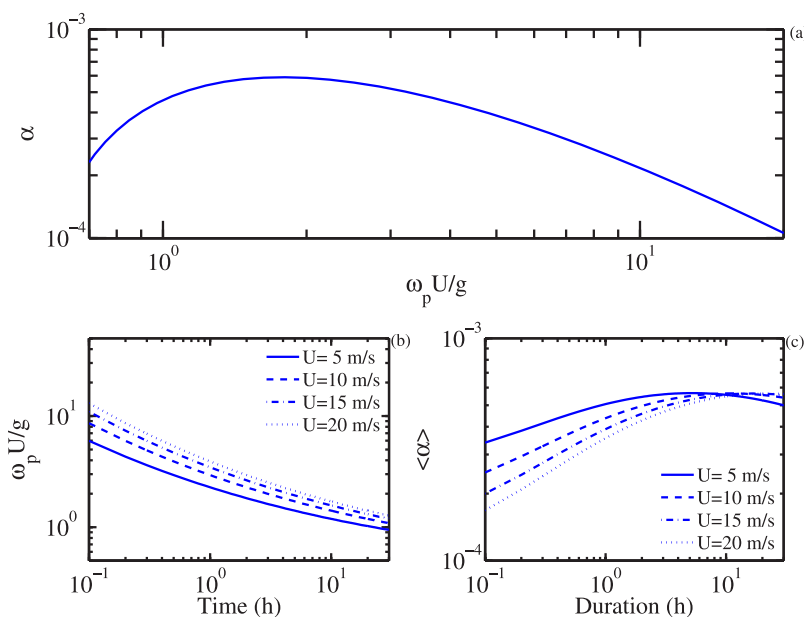


Figure 3. (a) Dependence of the energy dissipation coefficient on the dimensionless reference frequency. (b) The temporal variation of the dimensionless reference frequency of duration-limited wave growth. (c) The energy dissipation coefficient averaged over the duration of wind event plotted as a function of the wind event duration.

applications is $(3.7 \sim 5.7) \times 10^{-4}$. The rate of energy dissipation through the breaking process of wind-generated waves is therefore about 30 to 50% of the total wind power on the water surface estimated by $C_d \rho_a U^3$ with $C_d \approx 1.2 \times 10^{-3}$.

[20] Dissipation rate measurements in the ocean indicate that wave breaking is a significant process contributing to the turbulence properties in the upper ocean layer. Phillips [1985] presents a comprehensive discussion on the source and sink functions of the surface waves with special focus on wave breaking dissipation. The result leads to an analytical representation of the wave energy dissipation function based on an equilibrium wave spectrum argument. Using the analytical solution, the total energy dissipation of a wavefield can be easily computed. His solution approach is followed by Felizardo and Melville [1995] and Hanson and Philips [1999], both groups extend the calculation of energy dissipation using the in situ measured surface wave spectrum in addition to the assumed equilibrium spectral function defined by wind speed. Figure 4 reproduces Figure 8 of Hanson and Philips [1999] summarizing the results of energy dissipation as a function of wind speed in these two field campaigns. The experiment reported by Felizardo and Melville [1995] was conducted at the midlatitude in the Pacific Ocean (130 km west of Reedport, Oregon, in 3000 m of water) during 26 September – 7 October 1991, and that of Hanson and Philips [1999] was in the Gulf of Alaska (24 February – 1 March 1992) with considerably colder water temperature. The wind and wave conditions by Hanson and Philips [1999] are also much more variable in terms of mixed seas and wind steadiness. The data of Felizardo and Melville [1995] form an approximate upper bound of those of Hanson and Philips [1999], reflecting possibly the significant number of unsteady cases in the latter experiment. As discussed in the last paragraph, the parameterization function presented

in this paper suggests that the range of energy dissipation of wind-generated waves over the expected ocean conditions is estimated to be within a narrow range of $\varepsilon = (3.7 \sim 5.7) \times 10^{-4} \rho_a U^3$. As shown in Figure 4, these estimations are in very good agreement with the result of

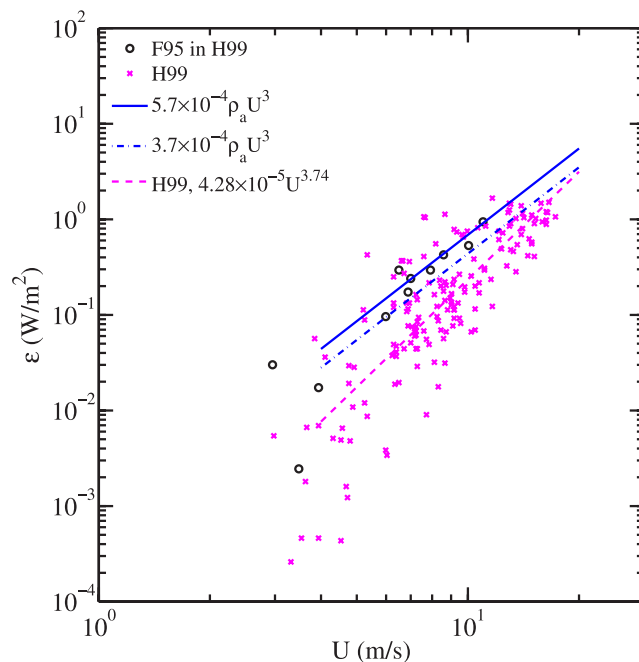


Figure 4. Comparison with wave energy dissipation measurements obtained from field experiments reported by Felizardo and Melville [1995] and Hanson and Philips [1999]; data points are reproduced from Figure 8 of Hanson and Philips [1999].

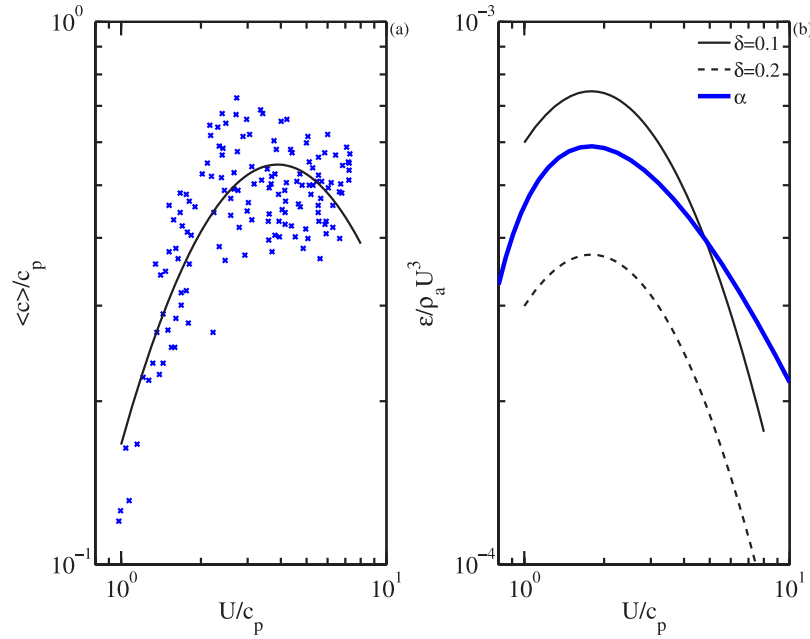


Figure 5. (a) Dependence of $\langle c \rangle / c_p$ on U / c_p (from Figure 6, Terray *et al.* [1996]). The solid curve is (18) derived from least squares fitting. (b) Comparison of $\varepsilon / \rho_a U^3$ based on integrating the vertical dissipation profile of Terray *et al.* [1996] to a depth of $z = -\delta H_s$ ($\delta = 0.1$ and 0.2) and α obtained in this study (15).

Felizardo and Melville [1995]. In unsteady wind events, the wave conditions would be much younger, resulting in a much smaller value of α and ε (Figure 3), as reflected in the data of Hanson and Philips [1999].

[21] Gemmrich and Farmer [2004] report near surface turbulence measurements in the presence of breaking waves using acoustic sensors mounted on a floating structure. They calculated the total dissipation integrated from the vertical profile of the turbulence distribution for a special case following several days of steady wind-forcing. The numerical values obtained from three different energy dissipation models are 6.5×10^{-4} , 8.8×10^{-4} and $9.0 \times 10^{-4} \text{ m}^3/\text{s}^3$ (p. 1084, Gemmrich and Farmer [2004]; their dissipation rate is per unit mass, the vertically integrated energy dissipation is defined as the equivalent of ε / ρ_a in this paper.) Using the wind speed of 12 m/s and $U / c_p = 1$ estimated from their Figure 4, the equivalent energy dissipation computed from our parameterization formula is $7.5 \times 10^{-4} \text{ m}^3/\text{s}^3$.

[22] Agrawal *et al.* [1992] and Terray *et al.* [1996] present vertical profiles of energy dissipation measurements derived from the velocity spectra obtained by laser Doppler anemometer, acoustic sensor and drag sphere. The results show a significant enhancement of the dissipation rate in the upper ocean layer due to surface wave breaking (about one to two orders of magnitude higher than that suggested by the wall layer similarity). The normalized vertical dissipation rate, ε_1 , can be expressed as (in the present notation that includes fluid density in the dissipation rate) [equation (9), Terray *et al.*, 1996]

$$\frac{\varepsilon_1 H_s}{\rho_a u_*^2 \langle c \rangle} = 0.3 \left(\frac{z}{H_s} \right)^{-2}, \quad (16)$$

where $\langle c \rangle$ is a velocity scale relating the surface wind stress and the rate of energy input to the waves from wind. The total energy dissipation can be integrated from (16) but the numerical value is critically determined by the upper limit of integration. The measured data only extend to about $z / H_s = -1$ so large uncertainty is expected from such an integration (here z is positive upward from the mean water surface). If we assume the vertical distribution of ε_1 continues to some depth near the water surface defined as $z = -\delta H_s$, where δ is less than one, we can take the integration to this depth to avoid a singular solution. The result can be written as

$$\frac{\varepsilon}{\rho_a U^3} = \frac{0.3 C_d \langle c \rangle c_p}{\delta c_p U} = \alpha_T, \quad (17)$$

The ratio $\langle c \rangle / c_p$ varies with U / c_p (reproduced from their Figure 6, with the friction velocity, u_* , converted to U in Figure 5a using $C_d = 0.0012$), and can be approximated by

$$\frac{\langle c \rangle}{c_p} = 0.1665 \left(\frac{U}{c_p} \right)^{1.749 - 0.6441 \ln(U / c_p)}. \quad (18)$$

Figure 5b plots α_T calculated with $\delta = 0.1$ and 0.2 in (17) together with α derived from the present analysis (15). From this comparison, it is suggested that the empirically observed z^{-2} vertical distribution of the energy dissipation function may extend to very close to the water surface and above the wave trough level ($z = -0.5 H_s$). It is further concluded that in order to reach an accurate account of the total energy dissipation in the ocean, it is necessary to be able to probe the very top layer of the ocean surface (to at least about $0.1 H_s$ below the mean water level). More extensive discussions of the vertical distribution of the

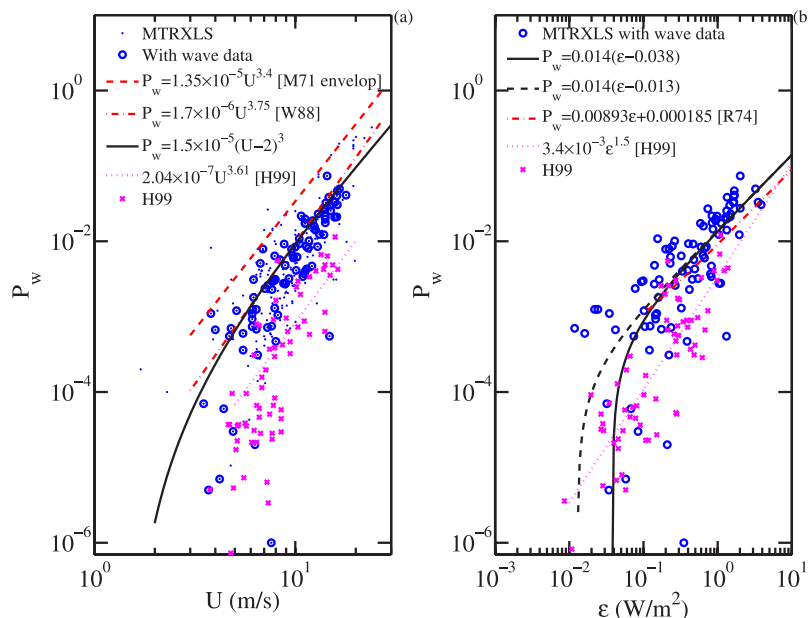


Figure 6. (a) Wind speed dependence of whitecap observations reproduced from the tables in MTRXLS [Monahan, 1971; Toba and Chaen, 1973; Ross and Cardone, 1974; Xu et al., 2000; Lafon et al., 2004, 2007; Sugihara et al., 2007]. (b) The dependence of whitecap coverage on surface wave energy dissipation.

energy dissipation function have been given elsewhere [e.g., Gemmrich and Farmer, 2004, and the references therein].

3. Application to Whitecap Observations

[23] Observations of whitecap coverage on the ocean surface are of great interest because whitecaps are probably the most conveniently observable indication of wave breaking, which plays an important role in air-sea interaction processes and ocean remote sensing applications. Many comprehensive reviews on the subject have been published [e.g., Monahan and O’Muircheartaigh, 1986; Anguelova and Webster, 2006; and the references therein]. The parameterizations of whitecap coverage, P_w , are usually given as power law functions of wind speed. Figure 6a shows the whitecap measurements reproduced from the tabulated data of Monahan [1971], Toba and Chaen [1973], Ross and Cardone [1974], Xu et al. [2000], Lafon et al. [2004, 2007] and Sugihara et al. [2007]; referred to as the MTRXLS data set from here on. Monahan [1971] suggests that $P_w = 1.35 \times 10^{-5} U^{3.4}$ forms an upper envelop of his whitecap measurements. The envelop function seems to be applicable to the assembled group of data also. The mean data trend follows very well the semi-analytical function $P_w = 1.7 \times 10^{-6} U^{3.75}$ suggested by Wu [1988]. Many more functions with somewhat slightly different coefficients have also been published. A table of 30 is given by Anguelova and Webster [2006]. Interestingly, when a threshold wind speed is introduced, a cubic wind speed relation,

$$P_w = 1.5 \times 10^{-5} (U - 2)^3 = 1.5 \times 10^{-5} U^3 - 1.2 \times 10^{-4}, \quad (19)$$

is found to fit the data equally well or better than equations using wind exponents different from cubic. This is especially true for the measurements in the lower wind

conditions (Figure 6a). Similar cubic wind speed relationship of whitecap coverage has been proposed by several researchers [e.g., Bondur and Sharkov, 1982; Monahan, 1993; Asher and Wanninkhof, 1998; Asher et al., 2002; Reising et al., 2002; Stramska and Petelski, 2003; see Table 1 of Anguelova and Webster, 2006].

[24] Water temperature or air-sea temperature difference appears to be the next important parameter affecting the whitecap coverage in the ocean. The Gulf of Alaska data measured by Monahan and reported by Hanson and Philips [1999] are also shown in Figure 6 for comparison. The whitecap coverage in cold water is about an order of magnitude less than those in more temperate waters. Many attempts to factor in wave parameters, such as wave age or dimensionless fetch, produce formulas that usually fit only selective data sets and it remains uncertain on how to properly account for explicit wave factors in whitecap observations.

[25] It is generally agreed that instead of wind speed, the wave energy dissipation is a better parameter to interpret the whitecap data because whitecaps are generated by breaking waves [e.g., Toba and Chaen, 1973; Ross and Cardone, 1974; Monahan and O’Muircheartaigh, 1986; Wu, 1988; Zhao and Toba, 2001]. Out of the 286 data points in MTRXLS, 103 are accompanied with report of significant wave height and peak wave frequency to facilitate dissipation computation as described in the last section. (The whitecap data under swell conditions by Sugihara et al. [2007] are not included in the dissipation computation here because the wave variance of the wind sea portion is not reported although the wind sea phase speed is listed in the tabulated data.) The result is shown in Figure 6b and the data can be represented by the power law function

$$P_w = 0.014(\varepsilon - \varepsilon_c). \quad (20)$$

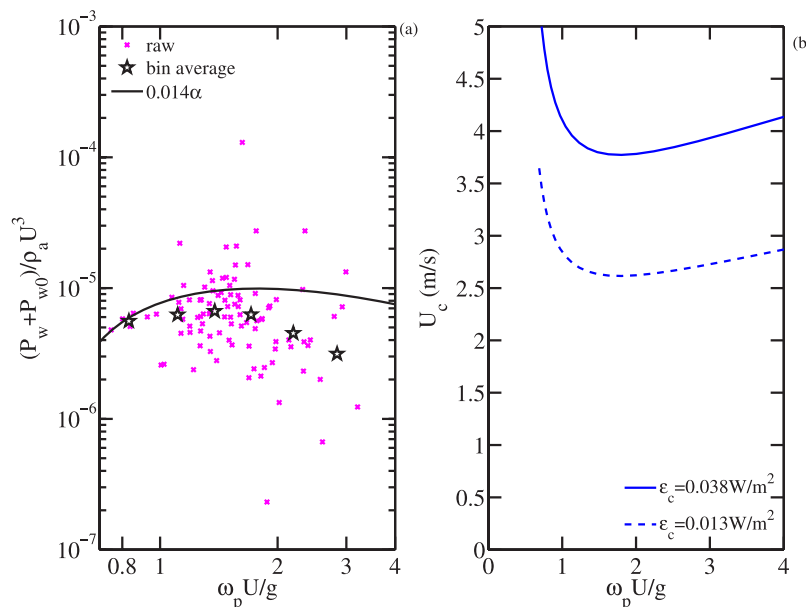


Figure 7. (a) Dependence of whitecap coverage on explicit wave parameters after the cubic wind speed dependence is removed. (b) The critical wind speed at whitecap inception estimated from the observed apparent energy dissipation threshold.

[26] The threshold energy dissipation for whitecap inception, ϵ_c , is between 0.013 and 0.038 W/m^2 judging from the data fitting. Ross and Cardone [1974] suggest a similar linear dependence between P_w and ϵ but the intercept of the linear function is positive ($P_w = 8.93 \times 10^{-3} \epsilon + 1.85 \times 10^{-4}$); that is, the threshold value of energy dissipation for whitecap inception in their equation is negative (whitecap presence in the absence of wind wave energy dissipation). Their equation is also shown in Figure 6b for comparison.

[27] The explicit wave properties are embedded in the α factor. As discussed in the last section and illustrated in Figure 3a, the numerical value of α is relatively unchanged over a broad range of wave development conditions (within a factor of about 2 for the range of ω_* , between 0.8 and 3, in the data of MTRXLS that also reported wave measurements; see Figure 7 later), and the influence is too weak to be clearly identified due to the large scatter of whitecap measurements (the whitecap data scatter is typically about one order of magnitude at a given wind speed). Figure 7a displays $(P_w - P_{w0})/\rho_a U^3$ to remove the strong cubic wind speed dependence in order to explore the dependence of whitecap coverage on wave parameters as suggested by (19) and (20), where P_{w0} is $0.014\epsilon_c$ and the mean value of the threshold dissipation rate (0.025 W/m^2) is used for ϵ_c . Similar to α , the data cloud of $(P_w - P_{w0})/\rho_a U^3$ display a non-monotonic trend as a function of ω_* . The local peak of the data cloud is near $\omega_* = 1.6$. Although the scatter is large, the resemblance of the local maximum of $(P_w - P_{w0})/\rho_a U^3$ and that of α (near $\omega_* = 1.8$) is encouraging in confirming that the dependence of whitecap coverage on the explicit surface wave parameter is about $\omega_*^{3.3} \eta_*$. Furthermore, because α is relatively constant, a cubic power law wind speed function (19) is equally robust for describing the whitecap coverage in the ocean given the nature of passive sensing that resulted in large data scatter (Figure 6).

[28] The data trend shown in Figure 6b suggests that there is a threshold dissipation level for visible whitecap inception; the numerical value of the threshold is between 0.013 and 0.038 W/m^2 . (The uncertainty in the proposed threshold value is due to the consideration that several low wind data points in Figure 6a do not have wave measurements for energy dissipation computation.) Substituting this value into the energy dissipation equation (15), the critical wind speed for whitecap inception as a function of wave development stage can be computed (Figure 7b). The variation of the critical wind speed is relatively insensitive to the stage of wave growth in the ω_* range between 1 and 4. The minimal critical wind speed is about 2.5 to 3.6 m/s and occurs near $\omega_* = 1.8$. This is in good agreement with the review by Monahan and O’Muircheartaigh [1986], who summarize in their abstract that “The wind speed associated with the onset of whitecapping, while also varying with ΔT and T_w , is typically 3 to 3.5 m s^{-1} , not the often quoted 7 m s^{-1} .” (ΔT and T_w are air-sea temperature difference and water temperature, respectively.) Whitecaps do occur under conditions with wind speed less than 3 m/s (see Figure 6a).

[29] Summarizing the above discussions, it becomes obvious that there is an apparent discrepancy of the threshold values used in the whitecap equations based on wind speed (19) and energy dissipation (20). It is quite likely that at lower wind conditions, other environmental factors modify the generation of wind waves, causing the wavefield to deviate from that predicted by the fetch- or duration-limited growth laws. The calculation of energy dissipation using (15) is therefore subject to larger uncertainty for low wind conditions.

4. Summary

[30] Using the robust fetch- or duration-limited growth functions of wind-generated waves, the net growth rate

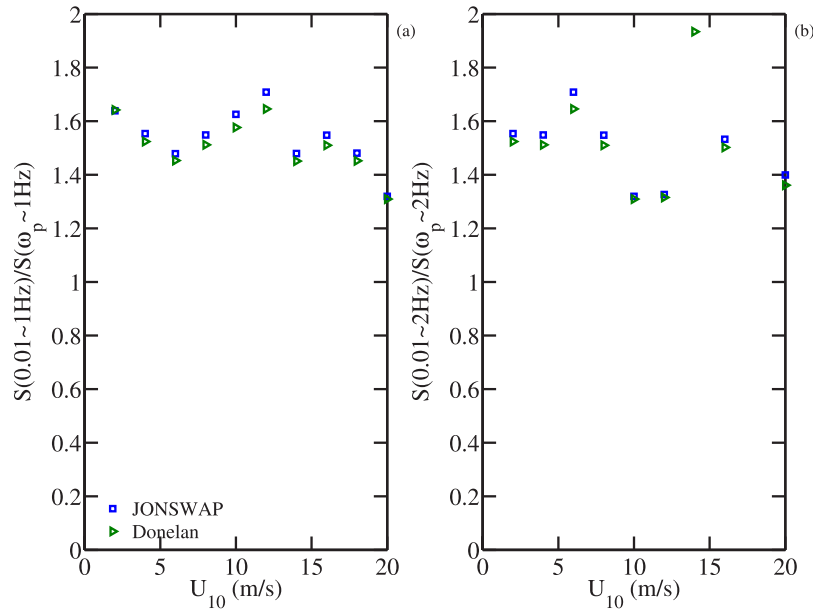


Figure A1. Correction factor accounting for the ratio of total variance used in $\langle \gamma \rangle$ and the fractional variance used in $\langle \gamma_e \rangle$.

of surface waves has been shown to be about one order of magnitude smaller than the integrated wind input [Hasselmann *et al.*, 1973; Donelan, 1998; and section 2.3]. The integrated dissipation function can therefore be approximated by the integrated wind input function. An analytical expression of the wind input and dissipation function is derived: $\varepsilon = \alpha \rho_a U^3$ with $\alpha = 0.20 \omega_*^{3.3} \eta_*$. The accuracy of α is estimated to be within about a factor of two. The uncertainty of the dissipation rate from the present approach is caused mainly by our imperfect knowledge of the wind input function and the short wave spectral function (Figure 1b). On the basis of this equation, the energy dissipation of surface waves per unit area of the ocean surface is proportional to the cubic power of wind speed and the explicit dependence of wave parameters is $\omega_*^{3.3} \eta_*$ (Figure 3a). Satellite remote sensing is now capable of providing global coverage of wind speed, significant wave height and dominant wave period. A parameterization equation such as the one given above can be used to generate a first-order estimation of the surface wave energy dissipation in the world's oceans. The surface wave energy dissipation represents the energy input from atmosphere to ocean and is an important upper (lower) boundary condition for the study of ocean (atmosphere) fluid dynamics.

[31] Applying the energy dissipation calculation to whitecap data that also reported wave measurements, the whitecap coverage as a function of surface wave energy dissipation is found to be $P_w = 0.014(\varepsilon - \varepsilon_c)$ with ε_c between 0.013 and 0.038 W/m². For a wide range of wave development conditions, α is almost constant. This may explain why it is very difficult to detect the dependence of whitecap coverage on explicit wave parameters. The MTRXLS data used for energy dissipation analysis in this paper can be described equally well by $P_w = 1.5 \times 10^{-5}(U-2)^3$ (Figure 6). Interestingly, the variation of α on ω_* is nonmonotonic. This property allows the weak wave signature to be detected in the whitecap data

with cubic wind dependence removed, that is, in the quantity P_w/U^3 (Figure 7a).

Appendix A: Numerical Computation of Wind Input Function

[32] The wind input function derived from field measurements [e.g., Snyder *et al.*, 1981; Hsiao and Shemdin, 1983; Donelan *et al.*, 2006] is for individual wave components. The net growth rate obtained from fetch- or duration-limited growth laws represents the result integrated over the full wave spectrum. In order to compare the two functions, an estimate of the integrated wind input function is calculated by

$$\langle \gamma_e \rangle = \frac{\int_{\omega_p}^{N\omega_p} \gamma s \omega \chi(\omega) d\omega}{s \omega_p \int_{\omega_p}^{N\omega_p} \chi(\omega) d\omega}. \quad (\text{A1})$$

Expressing the spectral function in the high frequency range above the spectral peak as $\chi(\omega) = A_s \omega^{-a_s}$, and denoting $\sigma = U/c = \omega U/g$, then for $\gamma_0 = B_0 \sigma^{b_0}$, (A1) becomes

$$\langle \gamma_0 \rangle = \gamma_{0p} \frac{(1 - a_s)(N^{b_0+2-a_s} - 1)}{(N^{1-a_s} - 1)(b_0 + 2 - a_s)}, \quad (\text{A2})$$

where $\gamma_{0p} = B_0 \sigma_p^{b_0}$, note that σ_p and ω_* are identical.

[33] For $\gamma_1 = B_1(\sigma - 1)^{b_1}$ and an arbitrary b_1 , the integration in the numerator of (A1) results in a solution in terms of the Gauss hypergeometric function. The numerical evaluation of the solution is rather cumbersome. On the basis of the experimental data, b_1 is 1.7 (equation (7)), which is between 1 and 2. Because simple solutions are available for $b_1 = 1$ and 2, the computation presented here is interpolated from the two particular solutions. Denoting

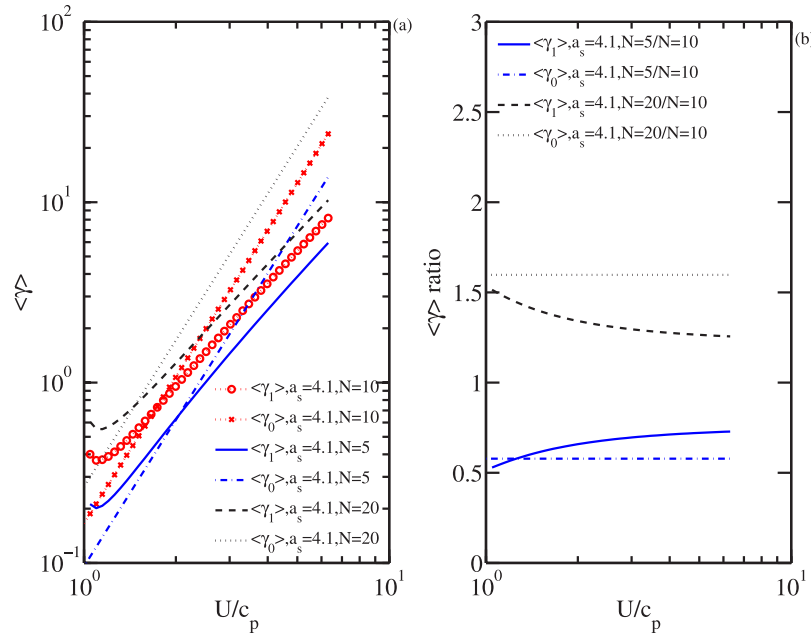


Figure A2. (a) Examples of the integrated wind input function computed with different fitting functions and spectral frequency bandwidths (represented by N). (b) The ratio of integrated wind input function computed with different spectral frequency bandwidths, with $N = 10$ as reference.

$\langle \gamma_1 \rangle_1$ as the integrated wind input function for $b_1 = 1$ and $\langle \gamma_1 \rangle_2$ for $b_1 = 2$, then

$$\langle \gamma_1 \rangle_1 = \gamma_{1p} \frac{(1 - a_s)}{(N^{1-a_s} - 1)} \left[\frac{N^{3-a_s} - 1}{3 - a_s} \sigma_p^2 - \frac{N^{2-a_s} - 1}{2 - a_s} \sigma_p \right], \text{ and} \quad (\text{A3})$$

$$\langle \gamma_1 \rangle_2 = \gamma_{1p} \frac{(1 - a_s)}{(N^{1-a_s} - 1)} \left[\frac{N^{4-a_s} - 1}{4 - a_s} \sigma_p^3 - 2 \frac{N^{3-a_s} - 1}{3 - a_s} \sigma_p^2 + \frac{N^{2-a_s} - 1}{2 - a_s} \sigma_p \right]. \quad (\text{A4})$$

where $\gamma_{1p} = B_1(\sigma_p - 1)^{b_1}$.

[34] In practical computations, the total wave variance is used for the parameterization of the source functions in this study. This introduces a correction factor of

$$\frac{\langle \gamma_e \rangle}{\langle \gamma \rangle} = \frac{\int_0^\infty \chi(\omega) d\omega}{\int_{\omega_p}^{N\omega_p} \chi(\omega) d\omega}. \quad (\text{A5})$$

The ratio of the total variance to the variance above the spectral peak is calculated using the JONSWAP and Donelan spectra [Hasselmann et al., 1973; Donelan et al., 1985]. As shown in Figure A1, this ratio is relative unchanging and a value of 1.6 is used in this study.

[35] Solutions (A3) and (A4) can be easily evaluated for a_s not equal to 1, 2, 3 or 4. Examples of computational results are shown in Figure A2 for $a_s = 4.1$ and 5. In (a), $\langle \gamma_0 \rangle$ and $\langle \gamma_1 \rangle$ computed for $N = 5, 10$ and 20 are graphed. The sensitivity to the frequency bandwidth of integration is

shown in (b). The wider the integration frequency bandwidth, the larger the numerical value of the proportionality coefficient of the dissipation rate. A better understanding of the physics of wave generation and dissipation will help in defining a more accurate value for the frequency range of integration.

[36] **Acknowledgments.** This work is supported by the Office of Naval Research (NRL Work Unit 6683 and 8953, and Program Element N61153 and N62435, NRL contribution number NRL/JA/7260—07-0160). We are grateful to the insightful comments from two anonymous reviewers.

References

- Agrawal, Y. C., E. A. Terray, M. A. Donelan, P. A. Hwang, A. J. Williams, W. M. Drennan, K. K. Kahma, and S. A. Kitaigorodskii (1992), High dissipation beneath surface waves due to breaking, *Nature*, *359*, 219–220.
- Angelova, M. D., and F. Webster (2006), Whitecap coverage from satellite measurements: A first step toward modeling the variability of oceanic whitecaps, *J. Geophys. Res.*, *111*, C03017, doi:10.1029/2005JC003158.
- Asher, W., and R. Wanninkhof (1998), The effect of bubble-mediated gas transfer on purposeful dual-gaseous tracer experiment, *J. Geophys. Res.*, *103*, 10,555–10,560.
- Asher, W., J. Edson, W. McGillis, R. Wanninkhof, D. Ho, and T. Litchendorf (2002), Fractional area whitecap coverage and air-sea gas transfer velocities measured during GasEx-98, in *Gas Transfer at Water Surfaces*, *Geophys. Monogr. Ser.*, vol. 127, edited by M. Donelan et al., pp. 199–204, AGU, Washington DC.
- Beranek, L. L. (1988), *Acoustic measurements*, American Institute of Physics, Cambridge, MA, 841 pp.
- Bondur, V., and E. Sharkov (1982), Statistical properties of whitecaps on a rough sea, *Oceanology*, *22*, 961–963.
- Dean, R. G., and R. A. Dalrymple (1991), *Water wave mechanics for engineers and scientists*, World Scientific Publ., 353 pp.
- Donelan, M. A. (1998), Air-water exchange processes, in *Physical Processes in Lakes and Oceans*, edited by J. Imberger, Coastal and Estuarine Studies Volume 54, 19–36, American Geophysical Union.
- Donelan, M. A., and W. J. Pierson (1987), Radar scattering and equilibrium ranges in wind-generated waves with application to scatterometry, *J. Geophys. Res.*, *92*, 4971–5029.
- Donelan, M. A., J. Hamilton, and W. H. Hui (1985), Directional spectra of wind-generated waves, *Philos. Trans. R. Soc.*, *A315*, 509–562.

- Donelan, M. A., M. Skafel, H. Graber, P. Liu, D. Schwab, and S. Venkatesh (1992), On the growth rate of wind-generated waves, *Atmos. Ocean*, *30*, 457–4782.
- Donelan, M. A., A. V. Babanin, I. R. Young, and M. L. Banner (2006), Wave-follower field measurements of the wind-input spectral function. Part II: Parameterization of the wind input, *J. Phys. Oceanogr.*, *36*, 1672–1689.
- Felizardo, F., and W. K. Melville (1995), Correlations between ambient noise and the ocean surface wave field, *J. Phys. Oceanogr.*, *25*, 513–532.
- Gemmrich, J. R., and D. M. Farmer (2004), Near-surface turbulence in the presence of breaking waves, *J. Phys. Oceanogr.*, *34*, 1067–1086.
- Hanson, J. L., and O. M. Philips (1999), Wind sea growth and dissipation in the open ocean, *J. Phys. Oceanogr.*, *29*, 1633–1648.
- Hasselmann, K., et al. (1973), Measurements of wind-wave growth and swell decay during the Joint North Sea Wave Project (JONSWAP), *Dtsch. Hydrogr. Z., Suppl. A*, *8*(12), 95 pp.
- Hsiao, S. V., and O. H. Shemdin (1983), Measurements of wind velocity and pressure with a wave follower during MARSEN, *J. Geophys. Res.*, *88*, 9841–9849.
- Hwang, P. A. (2006), Duration- and fetch-limited growth functions of wind-generated waves parameterized with three different scaling wind velocities, *J. Geophys. Res.*, *111*, C02005, doi:10.1029/2005JC003180.
- Hwang, P. A., and D. W. Wang (2001), Directional distributions and mean square slopes in the equilibrium and saturation ranges of the wave spectrum, *J. Phys. Oceanogr.*, *31*, 1346–1360.
- Hwang, P. A., and D. W. Wang (2004), Field measurements of duration limited growth of wind-generated ocean surface waves at young stage of development, *J. Phys. Oceanogr.*, *34*, 2316–2326, (Corrigendum, *35*, 268–270, 2005).
- Lafon, C., J. Piazzola, P. Forget, O. Le Calve, and S. Despiau (2004), Analysis of the variations of the whitecap fraction as measured in a coastal zone, *Boundary Layer Meteorol.*, *111*, 339–360.
- Lafon, C., J. Piazzola, P. Forget, and S. Despiau (2007), Whitecap coverage in coastal environment for steady and unsteady wave field conditions, *J. Mar. Syst.*, *66*, 38–46.
- Makin, V. K., V. N. Kudryavtsev, and C. Mastenbroek (1995), Drag on the sea surface, *Boundary Layer Meteorol.*, *73*, 159–182.
- Monahan, E. C. (1971), Oceanic whitecaps, *J. Phys. Oceanogr.*, *1*, 139–144.
- Monahan, E. C. (1993), Occurrence and evolution of acoustically relevant subsurface bubble plumes and their associated, remotely monitorable, surface whitecaps, in *Natural Physical Sources of Underwater Sound*, edited by B. Kerman, pp. 503–507, Springer, New York.
- Monahan, E. C., and I. G. O’Muircheartaigh (1986), Whitecaps and the passive remote sensing of the ocean surface, *Int. J. Remote Sens.*, *7*, 627–642.
- Phillips, O. M. (1985), Spectral and statistical properties of the equilibrium range in wind-generated gravity waves, *J. Fluid Mech.*, *156*, 505–531.
- Reising, S., W. Asher, L. Rose, and M. Aziz (2002), Passive polarimetric remote sensing of the ocean surface: The effects of surface roughness and whitecaps, paper presented at the International Union of Radio Science, Maastricht, Netherlands.
- Ross, D. B., and V. Cardone (1974), Observations of oceanic whitecaps and their relation to remote measurements of surface wind stress, *J. Geophys. Res.*, *79*, 444–452.
- Snyder, R. L., F. W. Dobson, J. A. Elliot, and R. B. Long (1981), Array measurement of atmospheric pressure fluctuations above surface gravity waves, *J. Fluid Mech.*, *102*, 1–59.
- Stramska, M., and T. Petelski (2003), Observations of oceanic whitecaps in the north polar waters of the Atlantic, *J. Geophys. Res.*, *108*(C3), 3086, doi:10.1029/2002JC001321.
- Sugihara, Y., H. Tsumori, T. Ohga, H. Yoshioka, and S. Serizawa (2007), Variation of whitecap coverage with wave-field conditions, *J. Mar. Syst.*, *66*, 47–60.
- Terray, E. A., M. A. Donelan, Y. C. Agrawal, W. M. Drennan, K. K. Kahma, A. J. Williams, P. A. Hwang, and S. A. Kitaigorodskii (1996), Estimates of kinetic energy dissipation under breaking waves, *J. Phys. Oceanogr.*, *26*, 792–807.
- Toba, Y., and M. Chaen (1973), Quantitative expression of the breaking of wind waves on the sea surface, *Rec. Oceanogr. Works Jpn.*, *12*, 1–11.
- Wu, J. (1988), Variations of whitecap coverage with wind stress and water temperature, *J. Phys. Oceanogr.*, *18*, 1448–1453.
- Xu, D., X. Liu, and D. Yu (2000), Probability of wave breaking and whitecap coverage in a fetch-limited sea, *J. Geophys. Res.*, *105*, 14,253–14,259.
- Zhao, D., and Y. Toba (2001), Dependence of whitecap coverage on wind and wind-wave properties, *J. Oceanogr.*, *57*, 603–616.

P. A. Hwang and M. A. Sletten, Remote Sensing Division, Naval Research Laboratory, Code 7264, BLDG. 2, Room 244E, 4555 Overlook Ave SW, Washington, DC 20375, USA. (phwang@ccs.nrl.navy.mil)